Materials Advances

ROYAL SOCIETY OF CHEMISTRY

REVIEW

View Article Online
View Journal | View Issue

Check for updates

Cite this: *Mater. Adv.*, 2023, 4, 5018

# Research progress on topological material-based photodetectors

Kewen Wu, Xiaoqi Liao, Muhammad Ahsan Iqbal and Yu-Jia Zeng *

Received 23rd July 2023,
Accepted 4th October 2023

DOI: 10.1039/d3ma00452j

rsc.li/materials-advances

Topological materials (TMs), namely topological insulators and semimetals, have unique physical properties, such as non-trivial surface states, linear electron dispersion, and high carrier mobility. Therefore, TMs appear promising in low-power and broad-spectrum photodetectors. This review provides an in-depth look at the current research in TM-based photodetectors. We critically discuss the growth methods and heterostructure fabrication of these emerging photodetectors. We also summarize the photodetecting performances of TMs, which allows us to better understand their strengths and weaknesses. Finally, challenges and perspectives on these emerging photodetectors are given, providing a foundation for further exploration of their great potential.

Open Access Article. Published on 04 2023. Downloaded on 20.10.24 7:31:28.
This article is licensed under a Creative Commons Attribution 3.0 Unported Licence.

## 1 Introduction

Photodetectors utilize the photoelectric effect of semiconductors to convert optical signals into electrical signals, which find extensive applications in diverse fields, such as optical communications, image capturing, and optical testing.[1–6] The photoelectric effect is the phenomenon in which photons transfer their energy to the electrons of a material when they strike its surface, causing the electrons to be emitted from atoms or molecules and forming electron–hole pairs. The generation of these charge carriers (electrons and holes) leads to the current flow, thereby producing an electrical signal proportional to the intensity of the incident light.

Photodetectors are characterized by several key parameters that are crucial for their performance.[7] One important parameter is responsivity ($R$), which indicates the ability of the photodetector to convert incident light into an electrical signal. $R$ can usually be calculated using

$$R = \frac{I_p - I_d}{PS} \quad (1)$$

where, $I_p$ represents the photocurrent, $I_d$ represents the dark current, $P$ is the incident light power density, and $S$ is the effective photosensitive surface area. Another important parameter is specific detectivity ($D^*$), which represents the sensitivity of the photodetector considering the noise characteristics.

*Key Laboratory of Optoelectronic Devices and Systems of Ministry of Education and Guangdong Province, College of Physics and Optoelectronic Engineering, Shenzhen University, Shenzhen 518060, China. E-mail: yjzeng@szu.edu.cn*

**Kewen Wu**

*Kewen Wu is a master's student at Shenzhen University. He received his bachelor's degree in Engineering from Xiamen University. His research interest is 2D semiconductor materials for optoelectronics.*

**Yu-Jia Zeng**

*Yu-Jia Zeng is a professor at Shenzhen University. He received his bachelor's degree in Materials Science and Engineering from Zhejiang University and his PhD degree in Materials Physics and Chemistry from Zhejiang University. After graduation, he worked at the Department of Physics of KU Leuven as a postdoctoral fellow and a research associate. His research interests include low-dimensional materials, in particular 2D materials, for optoelectronics and spintronics.*



© 2023 The Author(s). Published by the Royal Society of Chemistry

Open Access Article. Published on 04 2023. Downloaded on 20.10.24 7:31:28.
This article is licensed under a Creative Commons Attribution 3.0 Unported Licence.

$D^*$ can usually be calculated using

$$D^* = R\sqrt{\frac{S}{2eI_d}} \quad (2)$$

where $R$ and $e$ represent responsivity and electronic charge, respectively. Other parameters include response time, which measures the speed at which the photodetector can detect and respond to changes in light intensity, and detection range, which defines the range of light intensities the photodetector can effectively detect. These parameters collectively determine the overall effectiveness and suitability of the photodetector for specific applications. Ongoing technological advancements continuously drive the need for further improvements in these aspects of photodetectors.

Currently, the photodetectors available on the market are mainly made of inorganic semiconductor materials, such as Si, Ge, GaAs, HgCdTe, and others.[8–11] However, these materials have limitations, including their high cost and complicated fabrication process. In addition, due to band gap limitations, the photodetecting ability of these materials often only covers a specific wavelength range, with almost no optical response in the mid-to-far infrared and terahertz bands. To meet the growing demands, researchers are seeking new materials to develop photodetectors with more broad applications. Topological materials (TMs), with their unique physical properties such as non-trivial surface states, the quantum spin Hall effect,[12] three-dimensional quantum Hall effect,[13] zero bandgap topological structures,[14] and extremely high carrier mobility, have entered the field of photodetection. These characteristics enable TMs photodetectors to surpass the performance limitations of traditional inorganic semiconductor photodetectors, particularly in wide-spectrum photodetection and low-energy consumption devices. The detection range of some TM photodetectors can even reach THz, which far exceeds the detection limit of traditional semiconductor photodetectors. As TMs continue to advance, many researchers are exploring their applications in photodetectors. However, comprehensive reviews on this emerging topic are still very limited.

This review summarizes the current research status of several widely studied TMs in photodetectors, focusing on device fabrication methods and structures. Finally, the prospects of TMs in photodetectors are discussed based on the current development status.

## 2 Topological materials

TMs possess topological properties, with non-linear topological invariants in the bandgap region of their electronic structure. In TMs, the behavior of electrons is constrained and guided by spatial topology, giving rise to a range of unique physical phenomena and properties.[15–17] The electronic band structure of TMs is a crucial feature. For example, the energy ordering of the conduction and valence bands in regular insulator materials can be inverted by strong spin–orbit coupling (SOC), forming topological insulators (TIs).[18,19] In the case of TIs, as the strength of SOC gradually decreases, the bulk energy gap reduces until it reaches zero and then gradually increases. At the phase transition point, the conduction band minimum and valence band maximum intersect simultaneously in momentum space,[20] known as a topological semimetal (TSM)[21–23] (Fig. 1). Compared to ordinary materials, the band structure of TMs contains unconventional levels, such as band inversions, Dirac points, Weyl points, and so on. The presence of these unconventional levels is closely related to the topological invariants, resulting in unconventional physical properties. For example, the surface states of some TMs exhibit strong topological protection, making them highly stable against external disturbances and holding significant value for applications.[24]

TIs are unique materials that exhibit bulk insulating properties while conducting on their surfaces. Within a TIs, an electronic energy gap exists similar to that of a semiconductor. However, unlike semiconductors, TIs possess unique electronic states on their surfaces or edges. These particular surface states confine electrons to moving only along the material's surface or edge without penetrating the interior.[25,26] The surface states of TIs are safeguarded by time-reversal symmetry and spin-momentum locking, leading to enhanced carrier mobility and reduced energy losses. This feature makes TIs suitable for photodetectors, in which low power consumption and high response times are crucial factors. The highly unique electronic properties of the topologically protected boundary states make TIs promising in the energy sector in the future.

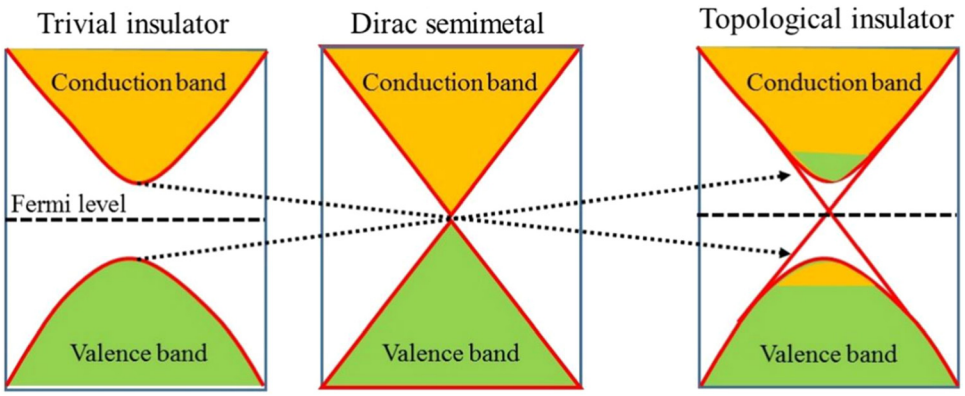


Fig. 1 The topological insulator (TI) and Dirac semimetal (DSM). Reprinted with permission from ref. 27. Copyright 2020, Springer Link.

Open Access Article. Published on 04 2023. Downloaded on 20.10.24 7:31:28.
This article is licensed under a Creative Commons Attribution 3.0 Unported Licence.

TSMs can be classified as Dirac semimetals (DSMs) and Weyl semimetals (WSMs).[28] In particular, this semimetal is a DSM if the conduction and valence bands meet at a single point and behave like massless Dirac fermions. When DSMs break the time or crystal symmetry, the corresponding Dirac fermion splits into two Weyl fermions[29] of opposite chirality, thus transforming into WSMs.[30–33] TSMs exhibit various exciting properties, such as extremely high carrier mobility, peculiar magnetic transport characteristics, and chiral edge modes.[32] Due to the linear dispersion and spin (pseudo-spin) momentum locking, low-energy electrons in TSMs exhibit strong robustness against crystal disorder and defects, resulting in very high electron mobility.[34,35] TSMs also exhibit significantly enhanced optical and photoelectric properties, such as the generation of large photocurrents,[36–39] second-harmonic generation,[40,41] optical activity, and gyrotropy.[42,43]

It is worth noting that the distinction between TIs and TSMs is not always straightforward, as some materials can exhibit characteristics of both.[44] For example, some TIs may exhibit metallic behavior in their surface states, while others may have a small but finite bandgap, making them similar to TSMs. The research on TMs is still rapidly evolving, and it is interesting to see what new materials and phenomena will be discovered in the coming years.

# 3 Photodetectors based on topological materials

The research of TM-based photodetectors has been an active field in recent years. The distinctive electronic band structure and topological properties of TMs have introduced entirely new possibilities for optoelectronic detection technology. Compared to traditional materials, TMs exhibit an array of unique characteristics, providing them with pronounced advantages in various specialized application domains. For instance, conventional photodetectors face limitations regarding high-speed response, low noise levels, and quantum effects. TM photodetectors achieve ultrahigh charge carrier mobility thanks to their specialized electron structure. As a result, they demonstrate considerable potential in high-speed detection. This attribute offers solutions for high-speed signal detection in fields such as optical communication and radar systems. Moreover, the distinctive distribution of electron states in TMs grants them exceptional low-noise properties, giving them an advantage in weak signal detection and precision measurement applications. In domains such as astronomical observation and biomedical imaging, TM photodetectors promise to achieve higher signal-to-noise ratios and more accurate measurements. TM photodetectors exhibit broad spectral absorption properties, enabling efficient photoelectric conversion across multiple wavelength ranges. This versatility makes them suitable for various applications, including spectroscopic analysis and imaging. Additionally, certain TMs display improved sensitivity to environmental changes. This feature opens up new possibilities in environmental monitoring, chemical sensing, and related fields.

Currently, TM photodetectors are mainly divided into two categories: TIs-based photodetectors, such as $Bi_2Se_3$-based photodetectors, and TSMs-based photodetectors, such as $Cd_3As_2$-based photodetectors. The preparation methods for TMs are diverse. Currently, standard fabrication methods are generally classified into bottom-up and top-down approaches. The bottom-up approaches mainly include van der Waals epitaxy, physical vapor deposition (PVD), chemical vapor deposition (CVD), molecular beam epitaxy (MBE), and pulsed laser deposition (PLD). The top-down approaches mainly include mechanical exfoliation and liquid-phase exfoliation. Each method has its advantages and disadvantages, leading to variations in the performance of the prepared photodetectors.[45] Also, two-dimensional (2D) forms of TMs have unique optical and electrical properties that make them uniquely advantageous in photodetection. For example, 2D TMs have a high surface electron density and strong interlayer resonance, which leads to strong optical absorption and efficient photoelectric conversion efficiency. In addition, 2D TMs have good optical linear and non-linear properties, which make them effective as optical detectors. In addition, the thin-film form of 2D TMs is easy to prepare and package, allowing for low-cost and high-efficiency photodetection. Therefore, many researchers have focused on 2D TMs for their photodetection properties.[46] Moreover, the construction of heterostructure can enhance the photodetecting performance of photodetectors. Consequently, many researchers have explored the photoelectric properties of heterostructures that combine TMs.

The research on TM photodetectors has achieved considerable results, for example, a significant improvement in photodetection efficiency, response speed, responsivity, *etc.* However, several challenges remain, such as growth quality control and stability issues. Therefore, there is still plenty of room for research on TM photodetectors.

## 3.1 Topological insulator photodetectors

The primary reason for the attention and development of TIs in photodetectors is their distinctive electronic structure. The topological surface states of these materials, constrained by both spin-coupling effects and time-reversal symmetry, exhibit small energy losses and high charge mobility. This makes them an ideal choice for developing low-power, high-response-rate electronic and optoelectronic devices.

In the photodetector domain, TIs primarily include $Bi_2Se_3$, $Bi_2Te_3$, $Sb_2Te_3$, and SnTe. Hence, this section will be centered around these core materials, providing a comprehensive summary of the research progress. Among these materials, $Bi_2Se_3$ is the pioneer to enter the field of photodetecting owing to its unique properties, such as high carrier mobility and a narrow 0.3 eV band gap. $Bi_2Se_3$ is a typical TI layered material with spin-locked Dirac cones in the outer layer and insulating band gaps in the inner layer. Observing along the *c*-axis (Fig. 2a),[47] the crystal structure of $Bi_2Se_3$ can be described as a layered compound composed of five atomic layers arranged in a repeating pattern. The stacking order is Se1–Bi–Se2–Bi–Se1, where ''1'' and ''2'' represent two distinct chemical states of the selenium anion.


© 2023 The Author(s). Published by the Royal Society of Chemistry

Open Access Article. Published on 04 2023. Downloaded on 20.10.24 7:31:28.
This article is licensed under a Creative Commons Attribution 3.0 Unported Licence.

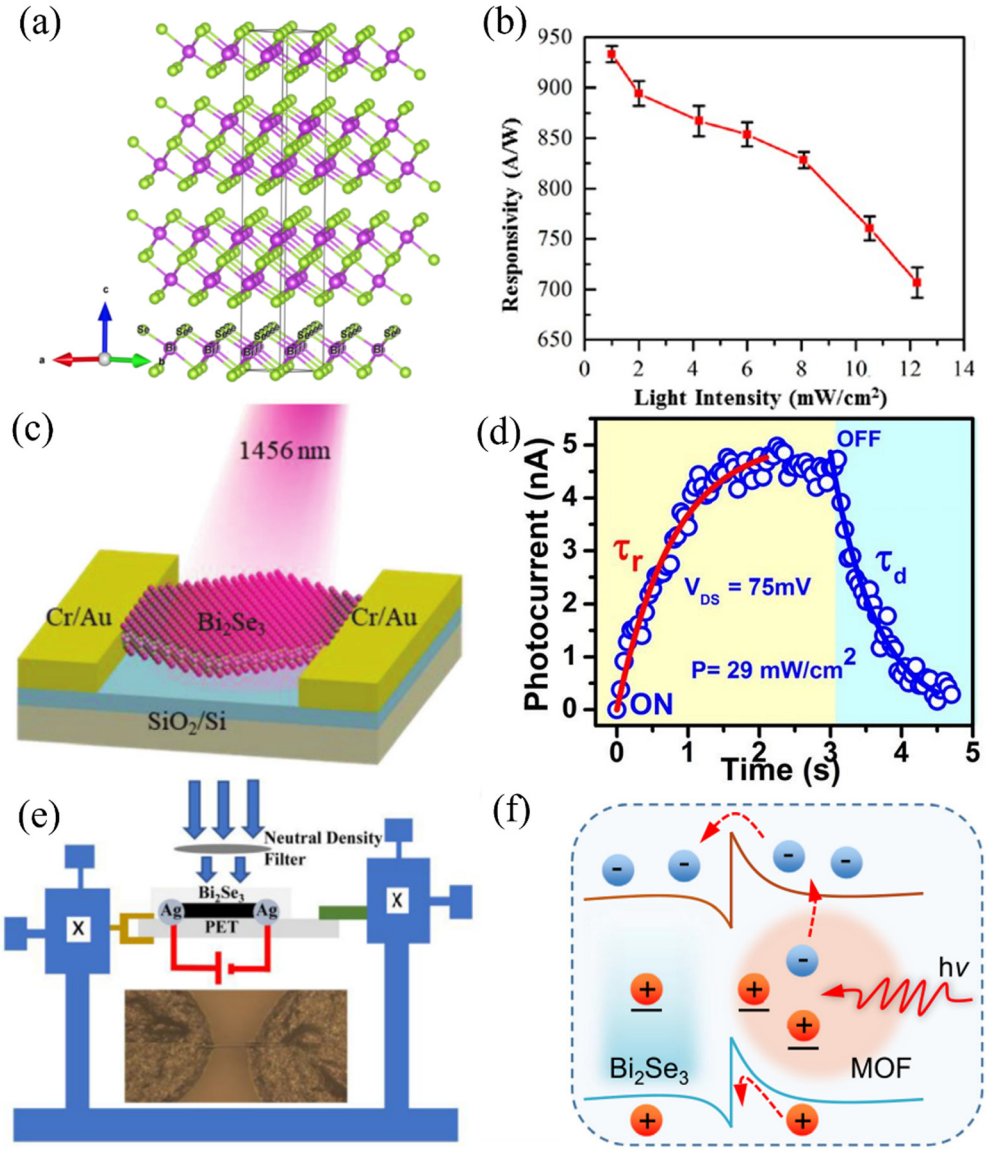


Fig. 2 (a) The schematic depiction showcases the crystal structures of $Bi_2Se_3$, where weak van der Waals interaction connects the quintuple layers. In the illustration, purple represents Bi atoms, while green represents Se atoms. Reprinted with permission from ref. 47. Copyright 2021, Elsevier. (b) Responsivities of $Bi_2Se_3$/Si nanowire near-infrared photodetector under different NIR intensities. Reprinted with permission from ref. 48. Copyright 2017, American Chemical Society. (c) $Bi_2Se_3$ photodetector on Si/$SiO_2$ substrate. Reprinted with permission from ref. 49. Copyright 2018, Wiley. (d) The response and decay times of the $Bi_2Se_3$ nanowire device. Reprinted with permission from ref. 50. Copyright 2014, Nature. (e) The experimental arrangement used to investigate the strain modulation effect in $Bi_2Se_3$ NWs. The inset within the figure displays an optical microscope image of the PD. Reprinted with permission from ref. 51. Copyright 2019, Elsevier. (f) Schematic band diagram of the $Bi_2Se_3$/MOF hybrid heterojunction under illumination. Reprinted with permission from ref. 52. Copyright 2022, Springer Nature.

Biswajit Das *et al.*[48] have prepared a $Bi_2Se_3$ nanosheet/Si nanowire heterojunction near-infrared detector using green, environmentally friendly, and cost-effective chemical technology. Fig. 2b shows the variation of $R$ with light intensity in $Bi_2Se_3$ heterojunction devices. The maximum $R$ and $D^*$ are 934.1 A $W^{-1}$ and 2.30 $\times$ $10^{13}$ Jones (at $\pm$0.5 V). Wang *et al.*[49] successfully prepared $Bi_2Se_3$ thin films using van der Waals epitaxy (VDWE) on graphene and investigated the optical properties of photoconductive detectors based on these thin films. As shown in Fig. 2c, under the illumination of 1456 nm light, the switching ratio, $R$, and external quantum efficiency (EQE) are as high as 972.5, 23.8 A $W^{-1}$ (at 1.0 V), and 2035%, respectively. Although the $R$ is lower than that of the nano-heterojunction device,[48] its detection range is larger. The research on $Bi_2Se_3$ thin film devices for photodetecting has been successful, and the study of its nanowire devices in photodetecting has also garnered much attention. Sharma *et al.*[50] obtained nanowires (NWs) by micromechanical exfoliation (ME) of the $Bi_2Se_3$ film, followed by further processing using a focused ion beam (FIB). The fabricated NW device shown in Fig. 2d exhibited photoelectric response across the visible to infrared light range. Under 1064 nm light, the $Bi_2Se_3$

Open Access Article. Published on 04 2023. Downloaded on 20.10.24 7:31:28.
This article is licensed under a Creative Commons Attribution 3.0 Unported Licence.

nanowire device had a $R$ up to 300 A $W^{-1}$ at a bias voltage of 0.075 V, with a rapid rise/decay in response time and good photocurrent repeatability. In addition to the influence of preparation methods on the photodetecting performance of devices, the performance of the devices can also be controlled through defects, applied strain, and doping. Wang *et al.*[51] utilized CVD to fabricate $Bi_2Se_3$ NWs. The device exhibited a $R$ of 191.75 mA $W^{-1}$ and a $D^*$ of $6.6 \times 10^{10}$ Jones under 442 nm illumination at the bias voltage of 2.0 V. They observed that upon introducing external compressive strain (Fig. 2e), the $I_p$ and $R$ of the device increased by 97% and 503%, respectively. According to their study, the strain modulation effect under compressive strain reduces the Schottky barrier height (SBH) and junction resistance, facilitating the transfer of photo-excited charge carriers and enhancing the photodetecting performance of the device. Therefore, strain modulation of nanoscale photodetectors through applied strain is a promising direction for future development. In another study, Zhai *et al.*[52] prepared a $Bi_2Se_3$/MOF heterojunction thin film high-performance infrared photodetector by hybridizing MOF with $Bi_2Se_3$ sheets. The MOF serves a dual role in the system. First, it functions as a photosensitive material, absorbing incident light. Additionally, it acts as a photogate layer, allowing it to control the conductance of the $Bi_2Se_3$ channel (Fig. 2f). The strong light absorption of MOF and the high carrier mobility of 2D $Bi_2Se_3$ sheets led to excellent photo response performance in the 500–2000 nm wavelength range. The $R$ and $D^*$ at 1500 nm found to be 4725 A $W^{-1}$ and $3.5 \times 10^{13}$ Jones at the bias voltage of 1.0 V, respectively, two to three orders of magnitude higher than those of the original $Bi_2Se_3$-based photodetectors. These studies have demonstrated the significant potential of $Bi_2Se_3$-based material for high-performance photodetectors. These findings indicate that $Bi_2Se_3$ heterojunction photodetectors show significant improvements in terms of $R$ and $D^*$ compared to previous single $Bi_2Se_3$ photodetectors.

$Bi_2Te_3$ is also a famous TM with high carrier mobility and a narrow band gap,[59] which has a broad development prospect in photodetection. $Bi_2Te_3$ is a well-studied thermoelectric

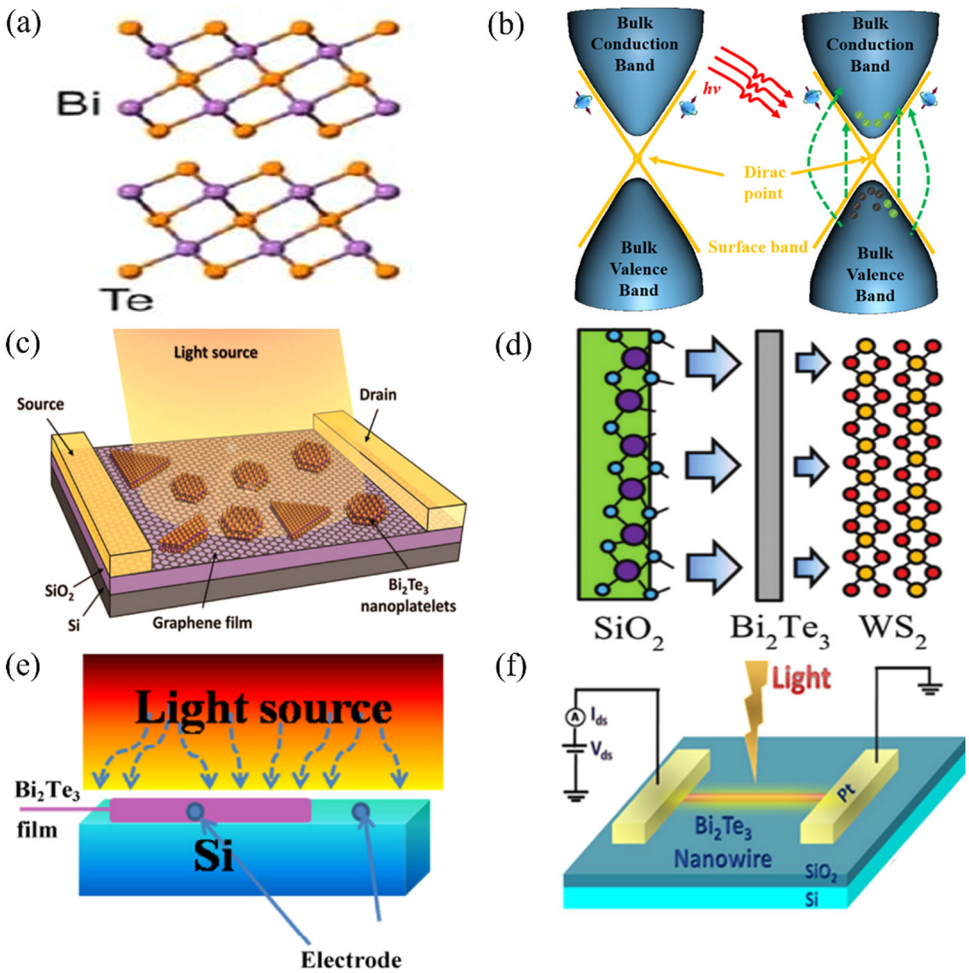


Fig. 3 (a) Schematic illustration of the $Bi_2Te_3$ crystal structures. Reprinted with permission from ref. 53. Copyright 2022, American Chemical Society. (b) Optical transition channels between $Bi_2Te_3$ bands. Reprinted with permission from ref. 54. Copyright 2017, Amer Inst Physcis. (c) Schematic of the graphene/$Bi_2Te_3$ heterostructure phototransistor device. Reprinted with permission from ref. 55. Copyright 2015, American Chemical Society. (d) The operational principle underlying the $WS_2$/$Bi_2Te_3$ photodetectors. Reprinted with permission from ref. 56. Copyright 2016, Royal Society of Chemistry. (e) Schematic of the n-$Bi_2Te_3$/p-Si junction structure. Reprinted with permission from ref. 57. Copyright 2017, Springer Nature. (f) Represents the schematics used for the photoelectric characterization. Reprinted with permission from ref. 58. Copyright 2017, American Chemical Society.


© 2023 The Author(s). Published by the Royal Society of Chemistry

Open Access Article. Published on 04 2023. Downloaded on 20.10.24 7:31:28.
This article is licensed under a Creative Commons Attribution 3.0 Unported Licence.

material.[60–62] It was not until recently, though, that its photodetecting capabilities were noticed. Like $Bi_2Se_3$, $Bi_2Te_3$ also has a layered structure bound by van der Waals forces, with five layers of atoms arranged along the *c*-axis and periodically stacked (Fig. 3a). Compared with $Bi_2Se_3$, $Bi_2Te_3$ has a smaller bulk band gap of 0.17 eV. Fig. 3b shows the energy band of $Bi_2Te_3$. Therefore, $Bi_2Te_3$ has attracted extensive attention in the field of long-wavelength photodetection. Liu *et al.*[54] fabricated single-crystal $Bi_2Te_3$ photodetectors on silicon by MBE, which showed a response from 1064–1550 nm. When the laser wavelength is 1550 nm, the *R* and internal quantum efficiency are $3.32 \times 10^{-2}$ A $W^{-1}$ and 7.4% at a bias voltage of 1.0 V, respectively. Under the irradiation of 1064 nm light, the *R* and internal quantum efficiency are $3.64 \times 10^{-3}$ A $W^{-1}$ and 0.9%, respectively.

Heterojunction devices composed of $Bi_2Te_3$ and other materials also exhibit good photoelectric properties. Qiao *et al.*[55] prepared a graphene/$Bi_2Te_3$ heterojunction-efficient photodetector by combining the ultrafine and broadband photoresponse properties of graphene with the excellent properties of $Bi_2Te_3$ in photodetecting (Fig. 3c). The device's *R* at 532 nm can reach 35 A $W^{-1}$ at the bias voltage of 1.0 V, and the photoconductance gain is up to 83. Yao *et al.*[56] prepared a $WS_2/Bi_2Te_3$ heterojunction photodetector to study the photodetecting performance of $WS_2$. As shown in Fig. 3d, the $Bi_2Te_3$ layer acts as a passivation layer. It shields the interference of $SiO_2$ on $WS_2$. Consequently, the device achieves an optical response range of 370–1550 nm with an *R* of 30.7 A $W^{-1}$ and a $D^*$ of $2.3 \times 10^{11}$ Jones at the bias voltage of 4.0 V. Wang *et al.*[57] prepared n-type $Bi_2Te_3$ films on p-type Si substrates by CVD (Fig. 3e). This heterojunction device showed good photoelectric properties. The material demonstrates a strong photovoltaic effect across a broad spectrum, from ultraviolet (UV) to near-infrared (NIR) wavelengths. Remarkably, it attained a short-circuit current of 19.2 μA and an open-circuit voltage of 235 mV when subjected to a 1000 nm wavelength. Additionally, the material exhibited rapid response times of only a few milliseconds. Yao *et al.*[63] prepared $Bi_2Te_3$–SnSe–$Bi_2Te_3$ photodetectors by combining 2D $Bi_2Te_3$ and SnSe. Because the energy band between $Bi_2Te_3$ and SnSe can be perfectly matched, the device has a good optical response in the range of UV to NIR (370–808 nm). After optimization, the *R* is 5.5 A $W^{-1}$, and the $D^*$ is $6 \times 10^{10}$ Jones at a bias voltage of 20.0 V. Sharma *et al.*[58] further investigated the photoelectric properties of $Bi_2Te_3$ NWs devices (Fig. 3f). They fabricated nanowire devices by FIB milling. Under near-infrared laser irradiation, the optical *R* of the NWs device is 780 A $W^{-1}$ and $D^*$ is $1.2 \times 10^9$ Jones at the bias voltage of 0.3 V. In addition, Sharma *et al.* also confirmed that the photodetecting performance of the device was hardly affected after 4 months in ambient conditions, which showed the superior stability of the $Bi_2Te_3$ NWs device.

Unlike other TIs, SnTe has a highly symmetrical crystal structure thus called a topological crystal insulator (TCI).[68] There is evidence that mirror symmetry protects the singular surface states of topological crystal insulators.[69,70] In addition, compared with other TMs, SnTe is easier to synthesize. These unique properties make SnTe a good research prospect in photodetection. In 2017, Gu *et al.*[64] prepared SnTe/Si photovoltaic

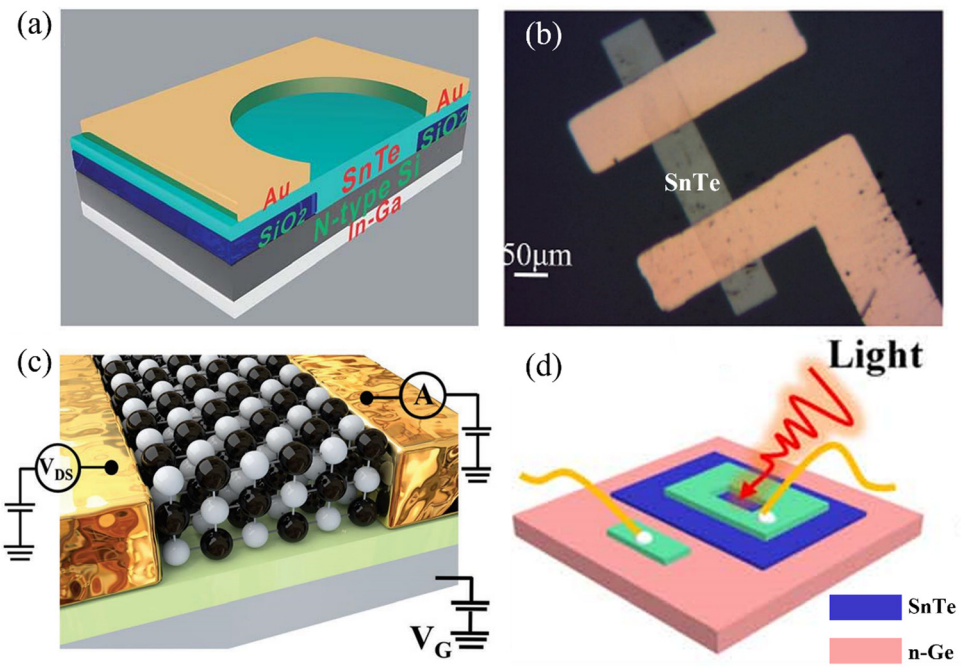


Fig. 4 (a) Photovoltaic detectors based on a heterostructure of SnTe/Si. Reprinted with permission from ref. 64. Copyright 2017, Royal Society of Chemistry. (b) OM image of the SnTe thin-film photodetector. Reprinted with permission from ref. 65. Copyright 2017, Wiley. (c) Schematic of the SnTe-based photodetector. Reprinted with permission from ref. 66. Copyright 2018, Wiley. (d) SnTe/n-Ge photovoltaic detector. Reprinted with permission from ref. 67. Copyright 2022, Institute of Physics Publishing.

Open Access Article. Published on 04 2023. Downloaded on 20.10.24 7:31:28.
This article is licensed under a Creative Commons Attribution 3.0 Unported Licence.

detectors (Fig. 4a) by CVD for the first time. The detector can realize light response in the wide spectral range of 254–1550 nm. Under 808 nm laser irradiation, the device exhibited the best light response, with a $D^*$ of $8.4 \times 10^{12}$ Jones and a switching ratio of $5 \times 10^6$ at a bias voltage of 0 V. Moreover, it has a fast response time, with a rise time of 8 μs and a fall time of 0.39 ms. However, this device requires high light intensity, and the light intensity significantly affects the photocurrent. Jiang *et al.*[65] fabricated the inaugural SnTe thin-film photodetector by MBE (Fig. 4b). The photodetector has a wide spectral response ranging from 405 nm–3.8 μm, with a $R$ of 3.75 A $W^{-1}$ at 2003 nm at a bias voltage of 2.0 V. Yang *et al.*[66] fabricated SnTe nanocrystal photodetectors directly on polyethylene terephthalate (PET) films in 2018 (Fig. 4c). The device has a broad spectral response (254–4650 nm). The $R$ can reach 71.11 A $W^{-1}$ under 254 nm at a bias voltage of 1 V. This detector can also exhibit the same light response on the flexible substrate. Therefore, it is expected to be well-developed in wearable devices. In 2022, Song *et al.*[67] prepared heterogeneous structures of SnTe and Ge using magnetron sputtering technology (Fig. 4d). The detector exhibits diode and photovoltaic characteristics in the visible to NIR band (400–2050 nm). Under 850 nm NIR illumination, the $R$ and $D^*$ of the photodetector reached a value of 0.62 A $W^{-1}$ and $2.33 \times 10^{11}$ Jones at a bias voltage of −0.5 V, respectively.

$Sb_2Te_3$ is also a typical TI. The band gap of $Sb_2Te_3$ is only 0.3 eV, and its carrier concentration and mobility are very high, at $10^{19}$–$10^{20}$ $cm^{-3}$ and 200 $cm^2$ $V^{-1}$ $s^{-1}$, respectively.[75] Because of these characteristics, $Sb_2Te_3$ has broad applications in photodetection. In 2015, Zheng *et al.*[71] studied the related performance of $Sb_2Te_3$ thin-film photodetectors (Fig. 5a). They successfully fabricated thin-film photodetectors through MBE. The bias voltage is set to be 1 V under 980 nm light, the $R$ is 21.7 A $W^{-1}$, the photoconductance gain is 27.4, and the switching ratio is 2.36. 2D p–n heterostructures are an essential research direction in integrated electronics and optoelectronics due to their unique physical, optical, and electrical properties.[76] $Sb_2Te_3$ is a p-type semiconductor, and finding a suitable n-type material in combination with $Sb_2Te_3$ could improve its photoelectric response. Si is an easily obtained n-type semiconductor, Yu *et al.*[72] fabricated a broadband self-powered photodetector based on $Sb_2Te_3$ and Si using photolithography and thermal evaporation technology. This detector has a fast response speed (<40 ms) and can realize photodetecting at 365–940 nm. By setting up an asymmetrical electrode structure, as shown in Fig. 5b, the detector can be self-powered for a broader range of applications. Zhang *et al.*[77] also prepared the $Sb_2Te_3$/n-Si heterojunction. They adopted the magnetron sputtering technology because of its lower cost and easier operation. After annealing, the detector can achieve a broad spectral response of 250–2400 nm, and the $R$ and $D^*$ can reach 270 A $W^{-1}$ and $1.28 \times 10^{13}$ Jones at 2400 nm at a bias voltage of 0.5 V. These performances are better than those of other reports, probably because annealing changes the crystallinity of the thin film. Sun *et al.*[73] prepared $Sb_2Te_3$ thin films on n-type $SrTiO_3$ (STO) substrates using MBE to constitute p–n heterojunction photodetectors (Fig. 5c). The detector can detect a wide spectrum from 405–1550 nm, and the switching ratio of the heterojunction device is $1.58 \times 10^6$ at 405 nm. Also, the rise

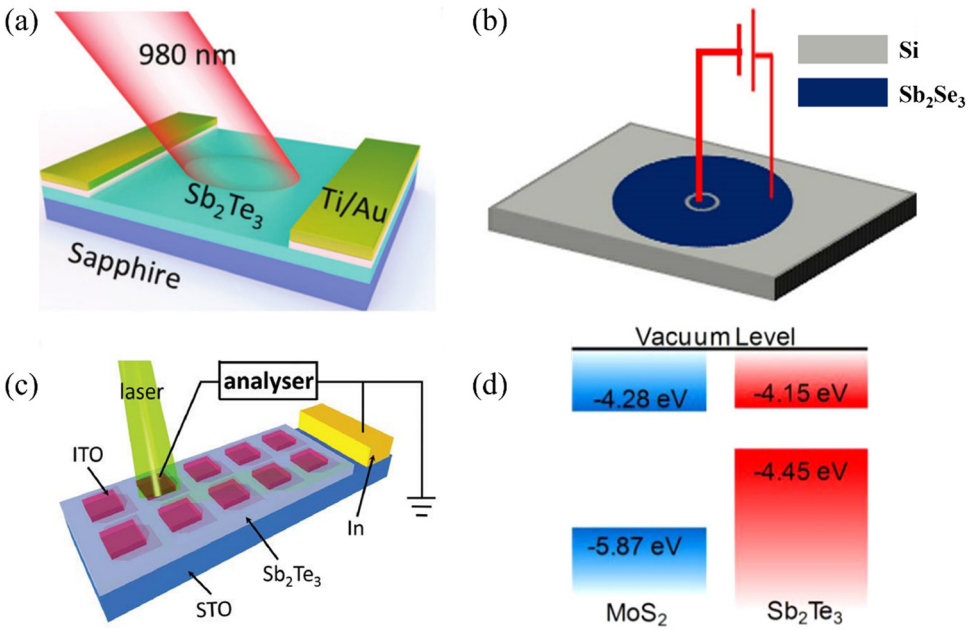


Fig. 5 (a) The schematic illustration of the $Sb_2Te_3$ film photodetector. Reprinted with permission from ref. 71. Copyright 2015, Royal Society of Chemistry. (b) Schematic representation of $Sb_2Te_3$ electrodes on a silicon substrate. Reprinted with permission from ref. 72. Copyright 2019, Institute of Physics Publishing. (c) The schematic diagram of the $Sb_2Te_3$ array photodetector and the measurement setup. Reprinted with permission from ref. 73. Copyright 2017, Royal Society of Chemistry. (d) Band structures of the achieved $Sb_2Te_3/MoS_2$ heterostructures. Reprinted with permission from ref. 74. Copyright 2019, Elsevier.


© 2023 The Author(s). Published by the Royal Society of Chemistry

Open Access Article. Published on 04 2023. Downloaded on 20.10.24 7:31:28.
This article is licensed under a Creative Commons Attribution 3.0 Unported Licence.

time is only 30 μs, and the fall time is 95 μs, faster than most other TI photodetectors. Liu *et al.*[74] successfully synthesized vertically stacked $Sb_2Te_3/MoS_2$ heterostructures by van der Waals epitaxial growth using the n-type material $MoS_2$. As shown in Fig. 5d, $Sb_2Te_3/MoS_2$ forms a type-II band alignment at the interface. The type-II band alignment effectively separates photo-excited charge carriers, enhancing the device's performance. Due to the distinctive band structure of the type-II band alignment heterojunction, it enables wide-band photoelectric response. This heterojunction has excellent photodetecting performance, with up to $10^6$ ultra-high current rectification rates and 4.5% photoelectric conversion efficiency. The $R$ reaches 330 A $W^{-1}$ by applying a negative voltage bias (−1 V) on the drain electrode, and the $D^*$ is $10^{12}$ Jones. This is one of the highest values of TI p–n junction photodetectors.

In addition to the aforementioned binary photodetectors, $Bi_2Te_2Se$ and $Sb_2SeTe_2$ and other ternary TMs have also entered the research scope. However, it is still in its infant stage. A few photodetectors with ternary topologies have been reported. In 2017, Huang *et al.*[78] studied the photodetecting performance of the $Sb_2SeTe_2$ nanoflake. In this study, $Sb_2SeTe_2$ showed remarkable performance. Under 532 nm wavelength illumination and a 1 V bias voltage, the $R$ and photoconductance gains reached 2293 A $W^{-1}$ and 5344, respectively. This is several orders of magnitude more responsive than previously reported TI photodetectors, suggesting that $Sb_2SeTe_2$ has great potential in the field of photodetectors. In 2021, G. K. Maurya *et al.*[79] integrated $Bi_2Te_2Se$ films and a silicon substrate to form a transverse heterojunction photodetector. Studies have shown that the $Bi_2Te_2Se$/Si heterojunction has a good photoelectric response in the range of visible light to near-infrared, and under 900 nm light, the $R$ is 19.06 A $W^{-1}$ under positive bias (+2 V), the $D^*$ is $8 \times 10^{11}$ Jones. The $R$ is 12.64 A $W^{-1}$ under reverse bias (−2 V), and the $D^*$ is $7.72 \times 10^{11}$ Jones. $Bi_2Te_2Se$ has now also been found to have promising applications in THz detection.[80]

Table 1 summarizes the key parameters and preparation methods of TI photodetectors in recent years. It can be seen that the long wave detection limit of TI photodetectors is approximately 5 μm away from the NIR band. Thin film and nanowire devices typically have better photodetecting performance owing to the advantages of nanoscale materials. In addition, the preparation method also has a significant impact on the photodetecting performance. For example, the $R$ of $Bi_2Se_3$ NW prepared by ME is three orders of magnitude higher than that prepared by CVD. Therefore, optimized nanostructures and preparation processes are crucial to improving photodetecting performances.

In photodetector application and development, the unique electronic structure of TIs gives them significant competitive edges compared to conventional materials. TIs demonstrate notably low energy losses and high charge mobility, laying a robust foundation for developing high-performance photodetectors. Additionally, the bandgap of TIs plays a crucial role in mitigating carrier recombination, further enhancing the sensitivity and response speed of detectors. Nevertheless, certain traditional materials may showcase superior optoelectronic performance within specific wavelength ranges. Hence, when selecting materials, it is essential to comprehensively consider the characteristics of different materials according to the specific requirements of the intended applications.

### 3.2 Topological semimetal photodetectors

With the progress of TMs, more TMs in the photodetecting field. In addition to the TIs discussed above, TSMs have gained attention recently. TSMs display a linear energy dispersion in their bulk state, where the conduction and valence bands intersect at topologically protected Dirac or Weyl nodes.[81] TSMs have many attractive physical properties, such as ultra-high

Table 1 Performances of topological insulator photodetectors

| Material | Synthesis method | Responsivity (A $W^{-1}$) | Detectivity (Jones) | Detection range (nm) | Ref. |
|---|---|---|---|---|---|
| $Bi_2Se_3$ NS/Si | — | $9.34 \times 10^2$ | $2.30 \times 10^{13}$ | NIR | 48 |
| $Bi_2Se_3$ film | VDWE | 23.8 | — | 1456 | 49 |
| $Bi_2Se_3$ NW | ME | $3 \times 10^2$ | — | Visible-infrared | 50 |
| $Bi_2Se_3$ NW | CVD | $1.92 \times 10^{-1}$ | $6.6 \times 10^{10}$ | 325–1064 | 51 |
| $Bi_2Se_3$/MOF | — | $4.725 \times 10^3$ | $3.5 \times 10^{13}$ | 500–2000 | 47 |
| $Bi_2Te_3$ | MBE | $3.32 \times 10^{-2}$ | — | 1064–1550 | 54 |
| Graphene/$Bi_2Te_3$ | — | $0.35 \times 10^2$ | 83 | UV-NIR | 55 |
| $WS_2/Bi_2Te_3$ | — | $0.307 \times 10^2$ | $2.3 \times 10^{11}$ | 370–1550 | 56 |
| $Bi_2Te_3$/Si | CVD | — | — | UV-NIR | 57 |
| $Bi_2Te_3$/SnSe/$Bi_2Te_3$ | — | 5.5 | $6 \times 10^{10}$ | 370–808 | 63 |
| $Bi_2Te_3$ NW | FIB | $7.8 \times 10^2$ | — | NIR | 58 |
| SnTe/Si | CVD | — | $8.4 \times 10^{12}$ | 254–1550 | 64 |
| SnTe film | MBE | 3.75 | — | 405–3.8 μm | 65 |
| SnTe/PET | — | $0.71 \times 10^2$ | — | 254–4650 | 66 |
| SnTe/Ge | PVD | 0.62 | $2.33 \times 10^{11}$ | 400–2050 | 67 |
| $Sb_2Te_3$ film | MBE | $0.22 \times 10^2$ | $1.22 \times 10^{11}$ | NIR | 71 |
| $Sb_2Te_3$/Si | PEP | — | — | 365–940 | 72 |
| $Sb_2Te_3$/Si | PVD | $2.7 \times 10^2$ | $1.28 \times 10^{13}$ | 250–2400 | 77 |
| $Sb_2Te_3$/STO | MBE | $4.8 \times 10^{-3}$ | $8.6 \times 10^{10}$ | 405–1550 | 73 |
| $Sb_2Te_3/MoS_2$ | CVD | $3.3 \times 10^2$ | $10^{12}$ | — | 74 |
| $Sb_2SeTe_2$ nanoflake | — | $2.29 \times 10^3$ | $4.5 \times 10^8$ | 532 | 78 |
| $Bi_2Te_2Se$/Si | — | $0.19 \times 10^2$ | $8 \times 10^{11}$ | Visible-infrared | 79 |

Open Access Article. Published on 04 2023. Downloaded on 20.10.24 7:31:28.
This article is licensed under a Creative Commons Attribution 3.0 Unported Licence.

electron mobility,[82] zero band gap, a topological Fermi arc, and the quantum Hall effect.[83–85] These physical properties extend the detectable spectral range of TSMs even to THz.[86] $Cd_3As_2$, $PtSe_2$, $PtTe_2$, $MoTe_2$ and $TaIrTe_4$ are the most studied TSMs. Other materials, such as $WTe_2$ and TaAs, also appear promising, even in their initial stages of research.

To date, the study of topological DSM photodetectors has mainly focused on $Cd_3As_2$. $Cd_3As_2$ is one of the first identified TSMs,[87] with a centrally symmetric tetragonal crystal structure.[88] Electronic structure calculations show that $Cd_3As_2$ is a 3D electronic analog of 3D DSM and graphene without spin splitting.[89] As early as 2013, Wang *et al.*[90] demonstrated through first-principle calculation and practical model analysis that $Cd_3As_2$ is a symmetrically protected TSM, paving the way for further studies. In a subsequent study, Liu *et al.*[91] confirmed this conclusion by directly observing a pair of 3D Dirac Fermions in $Cd_3As_2$ using angle-resolved photoelectron spectroscopy. Mosca Conte *et al.*[92] used density functional theory to study the electronic and optical properties of $Cd_3As_2$ and provided theoretical evidence for its potential use in wide-spectrum photodetecting. For their research on photodetectors, Wang *et al.*[93] employed CVD to synthesize $Cd_3As_2$ NWs and nanoplate devices. The nanoplate devices exhibited enhanced photoelectric response characterized by relatively low resistance and high carrier mobility. With a $R$ of 5.9 mA $W^{-1}$, it was shown that the response capabilities could span the wavelength range of 532 nm to 10.6 μm. These findings highlight the promising potential of $Cd_3As_2$ in photodetector components. Compared to submicron-structured photodetectors, their thin-film-based counterparts typically offer a higher photocurrent response owing to their larger photosensitive area, affording more pronounced detection advantages. In 2021, Yao *et al.*[94] employed the MBE technique to fabricate $Cd_3As_2$ thin films, extending the $Cd_3As_2$ photodetecting range into the THz frequency regime. They successfully realized room-temperature detection of THz waves utilizing $Cd_3As_2$, exhibiting high sensitivity, low energy requirements, and rapid response characteristics.

However, semimetal has an intrinsic ultra-high charge transfer rate and low resistance. Thus, even a small external bias can cause significant dark current, thereby limiting the device's performance, particular switch ratio and $D^*$. Building heterojunction photodetectors can effectively improve the photoelectric detector's performance. In 2018, Yang *et al.*[95]

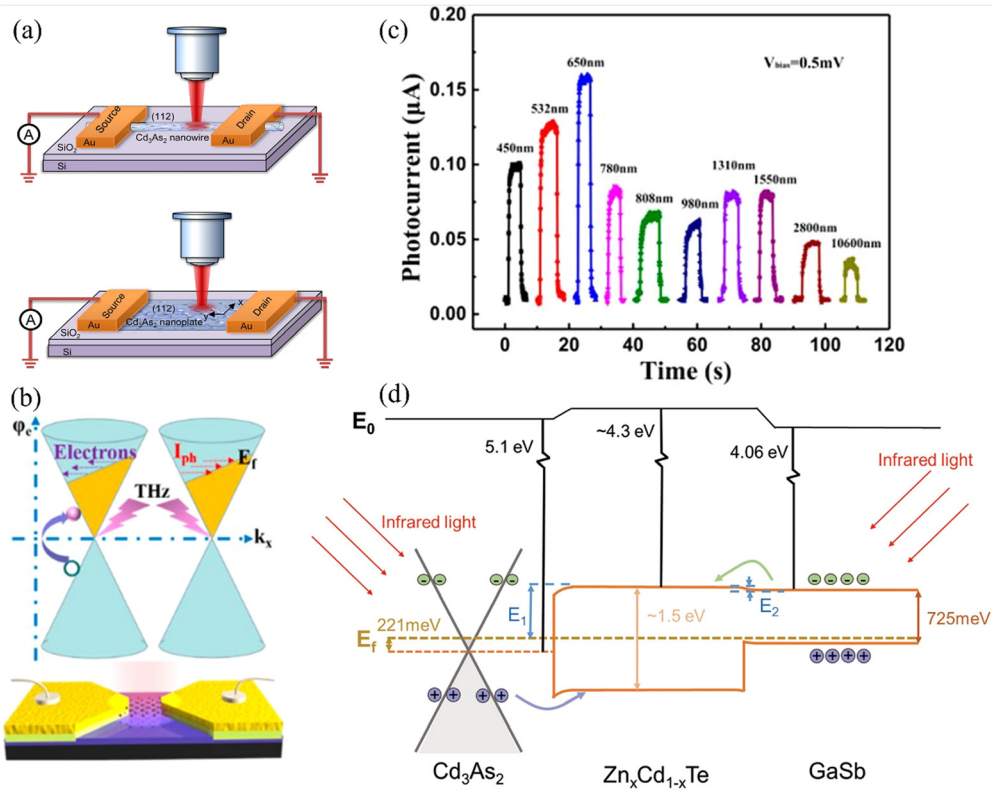


Fig. 6 (a) The diagram illustrates the scanning photocurrent measurement setup used for $Cd_3As_2$ nanowire and nanoplate devices. Reprinted with permission from ref. 93. Copyright 2017, American Chemical Society. (b) Schematic of the $Cd_3As_2$-based THz detector and photoconduction process of THz-excited Dirac fermions. Reprinted with permission from ref. 94. Copyright 2021, American Chemical Society. (c) Photocurrent curves of the $Cd_3As_2$ thin film/pentacene heterojunction photodetector with 0.5 V bias voltage. Reprinted with permission from ref. 95. Copyright 2018, American Chemical Society. (d) Band bending diagram with zero bias. Here, $E_0$, $E_f$, $E_1$, and $E_2$ represent the vacuum, Fermi, and the barrier heights between $Zn_xCd_{1-x}Te$ and $Cd_3As_2$ or GaSb, respectively. The electron affinity of the three layers and the bandgaps of $Zn_xCd_{1-x}Te$ and GaSb are also indicated. Upon illumination, the heterostructures experience photogeneration, generating electrons in GaSb and holes in $Cd_3As_2$. These photogenerated carriers migrate into the buffer layer, driven by the built-in electric field at the interfaces. The band diagram illustrates the direction of carrier movement, with the purple/green arrow indicating the direction of photogenerated holes/electrons. Reprinted with permission from ref. 97. Copyright 2022, American Chemical Society.


© 2023 The Author(s). Published by the Royal Society of Chemistry

Open Access Article. Published on 04 2023. Downloaded on 20.10.24 7:31:28.
This article is licensed under a Creative Commons Attribution 3.0 Unported Licence.

reported a broadband photodetector based on a $Cd_3As_2$ thin film/pentacene heterojunction. As shown in Fig. 6c, this photodetector can detect radiation wavelengths ranging from 450–10 600 nm at room temperature. Under illumination at 650 nm, it achieves a $R$ of 36.15 mA $W^{-1}$ at a bias of 0.5 mV. The outstanding performance of this photodetector in the long infrared wavelength range makes it promising in information communication. The combination of organic matter and thin film provides a new direction for studying $Cd_3As_2$ photodetection. Building upon this work, they substituted pentacene with small molecules and polymers,[96] expanding the detection range of $Cd_3As_2$-based photodetectors to 365–10 600 nm at bias zero. Moreover, the $R$ was significantly improved to 729 mA $W^{-1}$. In 2022, Yang *et al.*[97] realized the light response from the visible to the infrared band by constructing a double heterojunction. They prepared a wideband photodetector with $Cd_3As_2$/$Zn_xCd_{1-x}Te$/GaSb vertical heterostructure through simple and controllable magnetron sputtering and photolithography technology. They further demonstrated its imaging application, which makes the $Cd_3As_2$ heterostructure promising for practical devices.

$PtTe_2$ is a DSM with a $CdI_2$-type triangular (1T) structure, with six Te atoms surrounding each Pt atom.[98,99] In 2018, Xu *et al.*[100] reported a THz photodetector based on 2D $PtTe_2$. The device can be operated in self-powered mode. At zero bias, the $R$ is as large as 1.6 A $W^{-1}$ with a response time of less than 20 μs. At a bias of −100 mV, the $R$ can reach 3.8 A $W^{-1}$. In addition, they also constructed photodetectors based on graphene/$PtTe_2$ heterojunction, which can achieve a response time of less than 9 μs. In 2020, Tong *et al.*[101] reported successfully fabricating large-area $PtTe_2$ thin films through direct telluration of platinum. They developed $PtTe_2$/Si-based near-infrared photodetectors and image sensors based on these films. As shown in Fig. 7b, the photodetector exhibited a broadband response ranging from 200–1650 nm, with a maximum $R$ at 980 nm. Under illumination at 980 nm, the photodetector exhibited a $R$ and $D^*$ of 0.406 A $W^{-1}$ and 3.62 × $10^{12}$ Jones, respectively, with an EQE of up to 32.1% at zero bias.

Additionally, it demonstrated a very high response speed, with a rise time of only 7.51 μs and a fall time of 36.7 μs. The $PtTe_2$-based image sensor also exhibited excellent performance in infrared imaging. Wearable photodetectors have significant potential for diverse applications in imaging, sensing, optical communication, and environmental monitoring as photodetecting technology advances in the Internet of Things era.[104] Similar to the work of Tong, Shawkat *et al.*[102] directly fabricated a 2D $PtTe_2$ layer on a thin silicon wafer (Fig. 7c), enabling the fabrication of flexible 2D $PtTe_2$ photodetectors in the spectral range of 1–7 μm. This flexible detector demonstrated excellent photodetecting performance through extensive bending experiments, validating its potential for use in wearable photodetectors. This work significantly broadens the multifunctionality of Si-based photodetectors. In 2022, Yu *et al.*[103] successfully fabricated highly controllable wafer-scale $PtTe_2$/graphene 2D Dirac heterostructure photodetectors using CVD and photolithography techniques. The thickness and size of the devices

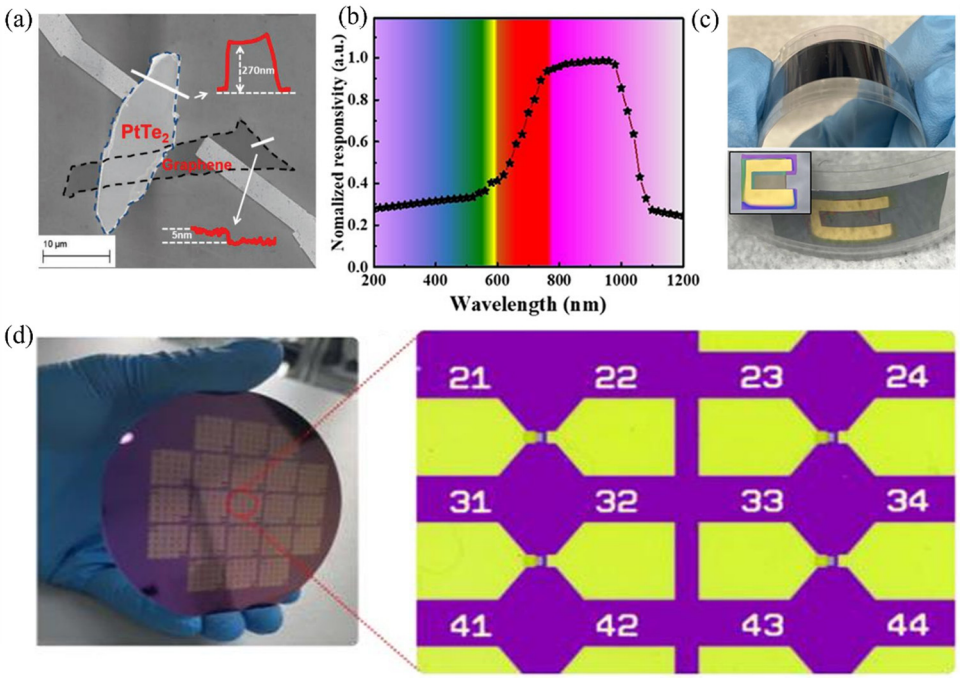


Fig. 7 (a)The SEM diagram of the device. Reprinted with permission from ref. 100. Copyright 2019, Wiley. (b) Normalized responsivity of the $PtTe_2$/Si NIRPD at zero bias. Reprinted with permission from ref. 101. Copyright 2022, American Chemical Society. (c) The top image showcases a thin Si wafer subjected to bending, while the bottom image displays a flexible 2D $PtTe_2$/Si photodetector. Reprinted with permission from ref. 102. Copyright 2021, American Chemical Society. (d) Large-scale $PtTe_2$/graphene photodetectors on a 4-in. wafer. Reprinted with permission from ref. 103. Copyright 2022, American Chemical Society.

Open Access Article. Published on 04 2023. Downloaded on 20.10.24 7:31:28.
This article is licensed under a Creative Commons Attribution 3.0 Unported Licence.

can be adjusted, and they are compatible with complementary metal–oxide–semiconductor (CMOS) technology (Fig. 7d). This fabrication method holds practical significance in integrated multifunctional photodetectors. The $R$ of the photodetector can reach 0.52 A $W^{-1}$ without bias, and $D^*$ can reach 2.58 × $10^{10}$ Jones.

$PtSe_2$ is a class DSM,[105] widely studied in photodetecting. Yu *et al.*[106] synthesized $PtSe_2$ by chemical vapor phase transport (CVT) and then prepared 2D $PtSe_2$ photodetectors by mechanical exfoliation. They found that the bilayer $PtSe_2$ devices were suitable for broadband mid-infrared photodetectors. The broadband range extends from visible to mid-infrared, with fast response and high sensitivity. In 2020, Feng *et al.*[107] studied the photoelectric properties of $PtSe_2$ and perovskite $CsPbX_3$ (X = Cl, Br, I) heterostructures. It showed through first-principle calculations that such heterostructures could improve the photoelectric carrier separation ability, broaden the absorption spectrum, and improve their photodetecting ability. Yang *et al.*[108] employed few-layer $PtSe_2$ to fabricate photodetector devices, with the primary mechanism for photocurrent generation being the photogating effect. This device exhibited an extremely high photoresponsivity and photocurrent, reaching a $R$ of 5 × $10^4$ A $W^{-1}$ at a bias voltage of 0.2 V. Moreover, they showed that the gate voltage can determine whether the device exhibits positive or negative photoconductance. Like $PtTe_2$ mentioned earlier, $PtSe_2$ can also be produced on a large scale through the direct sulfurization of Pt. Zeng *et al.*[109] utilized this method to construct a $PtSe_2$/Si NW. This device exhibited a $R$ of 12.65 A $W^{-1}$ at a bias voltage of −5 V, a $D^*$ of 2.5 × $10^{13}$ Jones, and an exceptionally high response speed. This array photodetector holds significant potential for future applications in optoelectronic and electronic devices.

Owing to its unique material properties, the WSM photodetector has an excellent sensitivity, broadband range, and self-powered operation performance. $MoTe_2$ is considered to be a possible WSM. Typically, $MoTe_2$ has three crystal structures: 2H, 1T′, and $T_d$ phases, in which 1T′ and 2H phases are trivial, $T_d$ phase is non-trivial.[111,112] Lai *et al.*[110] prepared a $T_d$-$MoTe_2$ broadband self-powered photodetector based on WSM's special unique material properties. The detector can not only achieve a broadband response of 532–10 600 nm (Fig. 8). Under 532 nm light irradiation, the device's $R$ can reach 0.40 mA $W^{-1}$, the $D^*$ is 1.07 × $10^8$ Jones at zero bias voltage, and the response time is 43 μs. However, despite the potential of WSMs in broadband photodetection, achieving large-scale synthesis for flexible devices remains a challenge. Notably, a significant breakthrough has recently been achieved in this regard. Through MBE techniques, Yang *et al.*[113] successfully grew centimeter-scale $T_d$-$MoTe_2$ films on flexible mica substrates. This result has introduced fresh possibilities for the application of $MoTe_2$ in the field of photodetection. It is worth emphasizing that the antenna-less, self-powered flexible photodetectors based on $T_d$-$MoTe_2$ exhibit outstanding performance. At room temperature, these detectors demonstrate remarkable electromagnetic radiation detection capabilities from ultraviolet to sub-millimeter wave regions and a rapid response time of approximately 20 microseconds. More notably, the detector's responsivity reaches 0.53 mA $W^{-1}$ (2.52 THz), with a NEP of 2.65 nW $Hz^{-0.5}$ (2.52 THz). These remarkable performance characteristics set $MoTe_2$ materials apart in photodetection, establishing a solid foundation for their application in wearable technology and other related domains.

Polarization-sensitive photodetecting has attracted much attention because of its unique applications. WSM also has a good development prospect in polarization-sensitive photodetecting. For example, the $MoTe_2$ broad spectrum self-powered photodetector[110] mentioned earlier also has an anisotropic response sensitive to the polarization angle. It exhibits an anisotropic response in the 532–10 600 nm range, with an anisotropic ellipse ratio up to 2.72 in the 10 600 nm band. Nevertheless, the intrinsic in-plane symmetry of the materials and the single structure of the detector impede the advancement of polarization detectors with high anisotropy ratios. $TaIrTe_4$ is a type-II WSM with an orthogonal structure and strong in-plane asymmetry. Therefore, $TaIrTe_4$ has attracted extensive attention in developing polarization-sensitive photodetectors. In 2018, Lai *et al.*[114] took the lead in constructing a photodetector based on $TaIrTe_4$, which could achieve a photoelectric response of 532–10 600 nm. Under

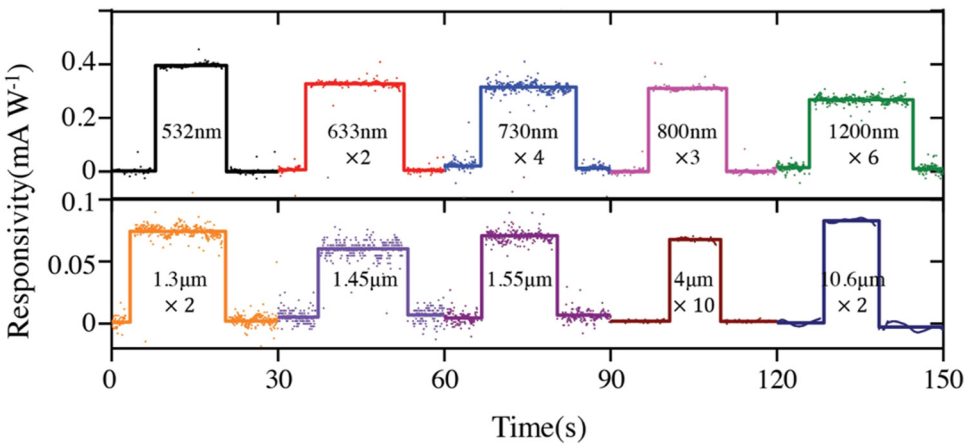


Fig. 8 Photocurrent response of the $MoTe_2$ device at different excitation wavelengths. Reprinted with permission from ref. 110. Copyright 2018, Wiley.


© 2023 The Author(s). Published by the Royal Society of Chemistry

Open Access Article. Published on 04 2023. Downloaded on 20.10.24 7:31:28.
This article is licensed under a Creative Commons Attribution 3.0 Unported Licence.

the irradiation of 10.6 μm light, the $R$ is 20 μA $W^{-1}$, and the $D^*$ is 1.8 × $10^6$ Jones at zero bias voltage. In addition, they demonstrated the anisotropic response of the $TaIrTe_4$ photodetector with polarized light. Its anisotropy ratios are 1.13, 1.56, and 1.88 at 633 nm, 4 μm, and 10.6 μm, respectively. It is not difficult to see that as the wavelength increases, the anisotropy becomes stronger. Han *et al.*[115] further constructed a $WSe_2$/$TaIrTe_4$/$MoS_2$ heterojunction photodetector in 2021. This heterojunction photodetector could achieve a wide spectral photoelectric response ranging from 405–1550 nm. At 635 nm wavelength, the device has a $R$ of 1.48 A $W^{-1}$ and a $D^*$ of $10^{11}$ Jones at zero bias. Its anisotropy ratio can be as large as 9.1, which is much improved compared to that of previously reported $TaIrTe_4$ photodetector.[114]

Table 2 summarizes the preparation methods and critical parameters of the TSM photodetectors. Compared with TI photodetectors, the detection limit of TSM photodetectors can reach 10 μm due to the zero gap and ultra-high carrier mobility of TSMs. Like TI photodetectors, the structure and preparation method significantly impact their performances.

TSMs, a distinctive class of functional materials, have demonstrated exciting potential. Their unique electronic band structure confers distinct advantages in photodetection. First, the electronic band structure of TSMs features peculiar band-crossing points between energy bands, generating highly sensitive band valleys that effectively enhance photovoltaic efficiency. Second, the fact that TSMs have different transport mechanisms, such as 0D, 1D, and 2D channels, makes it easier to separate and send carriers, which speeds up the photoresponse. Finally, TSMs exhibit a wide spectral response range, enabling them to detect a broader spectrum from ultraviolet to infrared wavelengths. Overall, TSMs present a remarkable outlook in photodetection, leveraging their distinctive electronic band structure and transport characteristics to forge new pathways for efficient photovoltaic conversion. Nevertheless, more in-depth research and work is needed to overcome the current issues with material synthesis and performance limitations. With these progresses, TSMs can be used in a wide range of optoelectronic devices.

# 4 Summary and outlook

In summary, we review the research progress of photodetectors based on TIs and TSMs. We summarize the performances of these emerging photodetectors, including responsivity, detectivity, response time, and detection wavelength. The aim is to provide researchers with a comprehensive understanding of the latest experimental advances in TMs for photodetection.

TMs have several advantages as photodetectors in many key performance aspects, such as high carrier mobility, excellent optical properties, and unique band structures. They show promising prospects in room temperature and wide-spectrum detection, particularly in the mid-to-far-infrared and THz regions. On the other hand, there are also certain limitations to TM-based photodetectors. One limitation is that the TM photodetector has a large dark current caused by the intrinsic band structure or surface states. The dark current will become even larger if impurities are present. The high dark current significantly restricts the application of TM-based photodetectors, as it can lead to high power consumption and noise.[116] Another limitation is the difficulty in producing high-quality TMs, especially for large-scale and low-cost synthesis.[24] Further research and technological advancements are needed to achieve controlled synthesis of high-quality, large-scale TMs at a low cost.

The research on TMs in photodetectors is still in its infant stage. Several research directions and prospects are outlined.

(1) Optimizing material quality and growth processes are of great importance to reduce the dark current. In particular, strict control of the stoichiometric ratio of TMs can suppress the generation of impurities and defects, thus reducing the dark current and noise. Also, selecting suitable materials and designing rational heterostructure and device structure can help to minimize the unintended current flow paths and improve the device's performance.

(2) Although progress has been made in synthesizing 2D TMs, achieving low-cost and large-scale fabrication still poses challenges. Therefore, further development of low-cost and reliable fabrication techniques, particularly for wafer-scale devices, is needed to drive the application of TMs in photodetection.

Table 2 Performances of topological semimetal photodetectors

| Material | Synthesis method | Responsivity (A $W^{-1}$) | Detectivity (Jones) | Detection range (nm) | Ref. |
|---|---|---|---|---|---|
| $Cd_3As_2$ nanoplate | CVD | 5.9 × $10^{-3}$ | — | 532–10 600 | 93 |
| $Cd_3As_2$ | MBE | 4 × $10^{-2}$ | — | THz | 94 |
| $Cd_3As_2$/pentacene | MBE | 3.6 × $10^{-2}$ | — | 450–10 600 | 95 |
| $Cd_3As_2$/organic | MBE | 0.729 | — | 365–10 600 | 96 |
| $Cd_3As_2$/$Zn_xCd_{1-x}Te$/GaSb | CVD | 0.216 | — | 520–2000 | 97 |
| $PtTe_2$ | — | 1.6 | — | — | 100 |
| $PtTe_2$/Si | CVD | 0.406 | 3.62 × $10^{12}$ | 200–1650 | 101 |
| $PtTe_2$/Si wafer | CVD | — | — | 1000–7000 | 102 |
| $PtTe_2$/graphene | CVD | 0.52 | 2.58 × $10^{10}$ | 405–1850 | 103 |
| $PtSe_2$ | CVT | | — | Visible-MIR | 106 |
| $PtSe_2$ | — | 5 × $10^4$ | — | — | 108 |
| $PtSe_2$/Si | — | 0.126 × $10^2$ | 2.5 × $10^{13}$ | 200–1550 | 109 |
| $MoTe_2$ | — | 0.40 × $10^{-3}$ | 1.07 × $10^8$ | 532–10 600 | 110 |
| $MoTe_2$ | MBE | 5.3 × $10^{-5}$ | — | UV-submm | 113 |
| $TaIrTe_4$ | — | 2 × $10^{-5}$ | 1.8 × $10^6$ | 532–10 600 | 114 |
| $WSe_2$/$TaIrTe_4$/$MoS_2$ | — | 1.48 | $10^{11}$ | 405–1550 | 115 |

Open Access Article. Published on 04 2023. Downloaded on 20.10.24 7:31:28.
This article is licensed under a Creative Commons Attribution 3.0 Unported Licence.

(3) Further study of interactions between photodetecting performances and different physical mechanisms will provide unprecedented opportunities to this field. First, TMs typically exhibit strong SOC, which is believed to play a critical role in polarization-sensitive photodetection and thus deserves further investigation. Second, introducing magnetism into the TI can break the time-reversal symmetry (TRS), thus creating a band gap in the surface state.[117,118] Therefore, magnetic doping or proximity with other magnetic materials, particularly 2D magnets,[119] should significantly impact the photodetecting performance. Finally, ferroelectric modulation of the photoelectric effect is one of the current research hotspots. The FE field effect can regulate carrier transport, increasing $R$ and $D^*$. It can also adjust the bandgap of 2D materials, increase the range of photodetecting, and effectively reduce the power consumption of photodetectors.[120,121]

In short, TMs possess numerous unique properties for applying novel photodetecting techniques. More advances and opportunities are expected in this emerging field.

## Conflicts of interest

There are no conflicts to declare.

## Acknowledgements

This work was supported by the National Natural Science Foundation of China (52273298 and 62250410366), the Guangdong Basic and Applied Basic Research Foundation (2022A1515010649) and the Shenzhen Science and Technology Program (JCYJ20210324095611032 and JCYJ20220818100008016).

## References

1 X. Lu, P. Jiang and X. Bao, *Nat. Commun.*, 2019, **10**, 138.
2 Y.-C. Chen, Y.-J. Lu, C.-N. Lin, Y.-Z. Tian, C.-J. Gao, L. Dong and C.-X. Shan, *J. Mater. Chem. C*, 2018, **6**, 5727–5732.
3 Y. Guo, Z. Xu, A. G. Curto, Y.-J. Zeng and D. Van Thourhout, *Prog. Mater. Sci.*, 2023, **138**, 101158.
4 M. Li, F. Yang, Y. Hsiao, C. Lin, H. Wu, S. Yang, H. Li, C. Lien, C. Ho, H. Liu, W. Li, Y. Lin and Y. Lai, *Adv. Funct. Mater.*, 2019, **29**, 1809119.
5 Y. Xin, J. Jiang, Y. Lu, H. Liang, Y. Zeng and Z. Ye, *Adv. Mater. Interfaces*, 2021, **8**, 2100058.
6 L. Hu, Q. Liao, Z. Xu, J. Yuan, Y. Ke, Y. Zhang, W. Zhang, G. P. Wang, S. Ruan, Y.-J. Zeng and S.-T. Han, *ACS Photonics*, 2019, **6**, 886–894.
7 J. Wang, J. Han, X. Chen and X. Wang, *InfoMat*, 2019, **1**, 33–53.
8 B. Cheng, C. Li, Z. Liu and C. Xue, *J. Semicond.*, 2016, **37**, 081001.
9 D. Marris-Morini, V. Vakarin, J. M. Ramirez, Q. Liu, A. Ballabio, J. Frigerio, M. Montesinos, C. Alonso-Ramos, X. Le Roux, S. Serna, D. Benedikovic, D. Chrastina, L. Vivien and G. Isella, *Nanophotonics*, 2018, **7**, 1781–1793.
10 N. Huo and G. Konstantatos, *Adv. Mater.*, 2018, **30**, 1801164.
11 J. Yuan, L. Hu, Z. Xu, Y. Zhang, H. Li, X. Cao, H. Liang, S. Ruan and Y.-J. Zeng, *J. Phys. Chem. C*, 2019, **123**, 14766–14773.
12 C. L. Kane and E. J. Mele, *Phys. Rev. Lett.*, 2005, **95**, 226801.
13 J. E. Moore and L. Balents, *Phys. Rev. B: Condens. Matter Mater. Phys.*, 2007, **75**, 121306.
14 S. Ouardi, C. Shekhar, G. H. Fecher, X. Kozina, G. Stryganyuk, C. Felser, S. Ueda and K. Kobayashi, *Appl. Phys. Lett.*, 2011, **98**, 211901.
15 C. Qu, Z. Zheng, M. Gong, Y. Xu, L. Mao, X. Zou, G. Guo and C. Zhang, *Nat. Commun.*, 2013, **4**, 2710.
16 B. Xu, Y. M. Dai, L. X. Zhao, K. Wang, R. Yang, W. Zhang, J. Y. Liu, H. Xiao, G. F. Chen, S. A. Trugman, J.-X. Zhu, A. J. Taylor, D. A. Yarotski, R. P. Prasankumar and X. G. Qiu, *Nat. Commun.*, 2017, **8**, 14933.
17 L. Zhang, Z. Chen, K. Zhang, L. Wang, H. Xu, L. Han, W. Guo, Y. Yang, C.-N. Kuo, C. S. Lue, D. Mondal, J. Fuji, I. Vobornik, B. Ghosh, A. Agarwal, H. Xing, X. Chen, A. Politano and W. Lu, *Nat. Commun.*, 2021, **12**, 1584.
18 B. Yan and C. Felser, *Annu. Rev. Condens. Matter Phys.*, 2017, **8**, 337–354.
19 Q. Wang, F. Wang, J. Li, Z. Wang, X. Zhan and J. He, *Small*, 2015, **11**, 4613–4624.
20 S. Murakami, *New J. Phys.*, 2008, **10**, 029802.
21 A. A. Soluyanov, D. Gresch, Z. Wang, Q. Wu, M. Troyer, X. Dai and B. A. Bernevig, *Nature*, 2015, **527**, 495–498.
22 N. P. Armitage, E. J. Mele and A. Vishwanath, *Rev. Mod. Phys.*, 2018, **90**, 015001.
23 S. M. Young, S. Zaheer, J. C. Y. Teo, C. L. Kane, E. J. Mele and A. M. Rappe, *Phys. Rev. Lett.*, 2012, **108**, 140405.
24 W. Tian, W. Yu, J. Shi and Y. Wang, *Materials*, 2017, **10**, 814.
25 Y. Guo, Z. Liu and H. Peng, *Small*, 2015, **11**, 3290–3305.
26 A. Junck, G. Refael and F. Von Oppen, *Phys. Rev. B: Condens. Matter Mater. Phys.*, 2013, **88**, 075144.
27 A. K. Pariari, *Indian J. Phys.*, 2021, **95**, 2639–2660.
28 N. P. Armitage, E. J. Mele and A. Vishwanath, *Rev. Mod. Phys.*, 2018, **90**, 015001.
29 H. Weyl, *Proc. Natl. Acad. Sci. U. S. A.*, 1929, **15**, 323–334.
30 S. M. Young, S. Zaheer, J. C. Y. Teo, C. L. Kane, E. J. Mele and A. M. Rappe, *Phys. Rev. Lett.*, 2012, **108**, 140405.
31 Z. Wang, Y. Sun, X.-Q. Chen, C. Franchini, G. Xu, H. Weng, X. Dai and Z. Fang, *Phys. Rev. B: Condens. Matter Mater. Phys.*, 2012, **85**, 195320.
32 A. A. Burkov and L. Balents, *Phys. Rev. Lett.*, 2011, **107**, 127205.
33 G. B. Halász and L. Balents, *Phys. Rev. B: Condens. Matter Mater. Phys.*, 2012, **85**, 035103.
34 T. Liang, Q. Gibson, M. N. Ali, M. Liu, R. J. Cava and N. P. Ong, *Nat. Mater.*, 2015, **14**, 280–284.
35 C. Shekhar, A. K. Nayak, Y. Sun, M. Schmidt, M. Nicklas, I. Leermakers, U. Zeitler, Y. Skourski, J. Wosnitza, Z. Liu, Y. Chen, W. Schnelle, H. Borrmann, Y. Grin, C. Felser and B. Yan, *Nat. Phys.*, 2015, **11**, 645–649.
36 H. Ishizuka, T. Hayata, M. Ueda and N. Nagaosa, *Phys. Rev. Lett.*, 2016, **117**, 216601.


© 2023 The Author(s). Published by the Royal Society of Chemistry

Open Access Article. Published on 04 2023. Downloaded on 20.10.24 7:31:28.
This article is licensed under a Creative Commons Attribution 3.0 Unported Licence.

37 K. Taguchi, T. Imaeda, M. Sato and Y. Tanaka, *Phys. Rev. B*, 2016, **93**, 201202.
38 G. B. Osterhoudt, L. K. Diebel, M. J. Gray, X. Yang, J. Stanco, X. Huang, B. Shen, N. Ni, P. J. W. Moll, Y. Ran and K. S. Burch, *Nat. Mater.*, 2019, **18**, 471–475.
39 C.-K. Chan, N. H. Lindner, G. Refael and P. A. Lee, *Phys. Rev. B*, 2017, **95**, 041104.
40 L. Wu, S. Patankar, T. Morimoto, N. L. Nair, E. Thewalt, A. Little, J. G. Analytis, J. E. Moore and J. Orenstein, *Nat. Phys.*, 2017, **13**, 350–355.
41 T. Morimoto and N. Nagaosa, *Sci. Adv.*, 2016, **2**, e1501524.
42 J. Ma and D. A. Pesin, *Phys. Rev. B: Condens. Matter Mater. Phys.*, 2015, **92**, 235205.
43 P. Goswami, G. Sharma and S. Tewari, *Phys. Rev. B: Condens. Matter Mater. Phys.*, 2015, **92**, 161110.
44 D. Culcer, A. Cem Keser, Y. Li and G. Tkachov, *2D Mater.*, 2020, **7**, 022007.
45 C. Yue, S. Jiang, H. Zhu, L. Chen, Q. Sun and D. Zhang, *Electronics*, 2018, **7**, 225.
46 J. S. Ponraj, Z.-Q. Xu, S. C. Dhanabalan, H. Mu, Y. Wang, J. Yuan, P. Li, S. Thakur, M. Ashrafi, K. Mccoubrey, Y. Zhang, S. Li, H. Zhang and Q. Bao, *Nanotechnology*, 2016, **27**, 462001.
47 F. K. Wang, S. J. Yang and T. Y. Zhai, *iScience*, 2021, **24**, 103291.
48 B. Das, N. S. Das, S. Sarkar, B. K. Chatterjee and K. K. Chattopadhyay, *ACS Appl. Mater. Interfaces*, 2017, **9**, 22788–22798.
49 F. Wang, L. Li, W. Huang, L. Li, B. Jin, H. Li and T. Zhai, *Adv. Funct. Mater.*, 2018, **28**, 1802707.
50 A. Sharma, B. Bhattacharyya, A. K. Srivastava, T. D. Senguttuvan and S. Husale, *Sci. Rep.*, 2016, **6**, 19138.
51 X. Wang, G. Dai, B. Liu, H. Zou, Y. Chen, X. Mo, X. Li, J. Sun, Y. Liu, Y. Liu and J. Yang, *Phys. E*, 2019, **114**, 113620.
52 F. Wang, J. Wu, Y. Zhang, S. Yang, N. Zhang, H. Li and T. Zhai, *Sci. China Mater.*, 2022, **65**, 451–459.
53 Q. Shi, J. Li, X. Zhao, Y. Chen, F. Zhang, Y. Zhong and R. Ang, *ACS Appl. Mater. Interfaces*, 2022, **14**, 49425–49445.
54 J. Liu, Y. Li, Y. Song, Y. Ma, Q. Chen, Z. Zhu, P. Lu and S. Wang, *Appl. Phys. Lett.*, 2017, **110**, 141109.
55 H. Qiao, J. Yuan, Z. Xu, C. Chen, S. Lin, Y. Wang, J. Song, Y. Liu, Q. Khan, H. Y. Hoh, C.-X. Pan, S. Li and Q. Bao, *ACS Nano*, 2015, **9**, 1886–1894.
56 J. Yao, Z. Zheng and G. Yang, *J. Mater. Chem. C*, 2016, **4**, 7831–7840.
57 Z. Wang, M. Li, L. Yang, Z. Zhang and X. P. A. Gao, *Nano Res.*, 2017, **10**, 1872–1879.
58 A. Sharma, A. K. Srivastava, T. D. Senguttuvan and S. Husale, *Sci. Rep.*, 2017, **7**, 17911.
59 Y. L. Chen, J. G. Analytis, J.-H. Chu, Z. K. Liu, S.-K. Mo, X. L. Qi, H. J. Zhang, D. H. Lu, X. Dai, Z. Fang, S. C. Zhang, I. R. Fisher, Z. Hussain and Z.-X. Shen, *Science*, 2009, **325**, 178–181.
60 O. V. Nitsovich and M. V. Serbyn, *Phys. Chem. Solid State*, 2018, **19**, 297–302.
61 P. Ngabonziza, *Nanotechnology*, 2022, **33**, 192001.
62 Y. Chen, X. Hou, C. Ma, Y. Dou and W. Wu, *Adv. Mater. Sci. Eng.*, 2018, **2018**, 1–9.
63 J. Yao, Z. Zheng and G. Yang, *Adv. Funct. Mater.*, 2017, **27**, 1701823.
64 S. Gu, K. Ding, J. Pan, Z. Shao, J. Mao, X. Zhang and J. Jie, *J. Mater. Chem. A*, 2017, **5**, 11171–11178.
65 T. Jiang, Y. Zang, H. Sun, X. Zheng, Y. Liu, Y. Gong, L. Fang, X. Cheng and K. He, *Adv. Opt. Mater.*, 2017, **5**, 1600727.
66 J. Yang, W. Yu, Z. Pan, Q. Yu, Q. Yin, L. Guo, Y. Zhao, T. Sun, Q. Bao and K. Zhang, *Small*, 2018, **14**, 1802598.
67 L. Song, L. Tang, Q. Hao, K. S. Teng, H. Lv, J. Wang, J. Feng, Y. Zhou, W. He and W. Wang, *Nanotechnology*, 2022, **33**, 425203.
68 T. H. Hsieh, H. Lin, J. Liu, W. Duan, A. Bansil and L. Fu, *Nat. Commun.*, 2012, **3**, 982.
69 L. Fu, *Phys. Rev. Lett.*, 2011, 4.
70 G. A. Fiete, *Nat. Mater.*, 2012, **11**, 1003–1004.
71 K. Zheng, L.-B. Luo, T.-F. Zhang, Y.-H. Liu, Y.-Q. Yu, R. Lu, H.-L. Qiu, Z.-J. Li and J. C. Andrew Huang, *J. Mater. Chem. C*, 2015, **3**, 9154–9160.
72 X.-X. Yu, Y. Wang, H. Zhang, D. Zhu, Y. Xiong and W. Zhang, *Nanotechnology*, 2019, **30**, 345202.
73 H. Sun, T. Jiang, Y. Zang, X. Zheng, Y. Gong, Y. Yan, Z. Xu, Y. Liu, L. Fang, X. Cheng and K. He, *Nanoscale*, 2017, **9**, 9325–9332.
74 H. Liu, D. Li, C. Ma, X. Zhang, X. Sun, C. Zhu, B. Zheng, Z. Zou, Z. Luo, X. Zhu, X. Wang and A. Pan, *Nano Energy*, 2019, **59**, 66–74.
75 S. K. Verma, K. Kandpal, P. Kumar, A. Kumar and C. Wiemer, *IEEE Trans. Electron Devices*, 2022, **69**, 4342–4348.
76 X. Pan, J. He, L. Gao and H. Li, *Nanomaterials*, 2019, **9**, 1771.
77 Y. Zhang, L. Tang and K. S. Teng, *Nanotechnology*, 2020, **31**, 304002.
78 S.-M. Huang, S.-J. Huang, Y.-J. Yan, S.-H. Yu, M. Chou, H.-W. Yang, Y.-S. Chang and R.-S. Chen, *Sci. Rep.*, 2017, **7**, 45413.
79 G. K. Maurya, F. Ahmad, S. Kumar, V. Gautam, K. Kandpal, A. Tiwari and P. Kumar, *Appl. Surf. Sci.*, 2021, **565**, 150497.
80 P. Seifert, K. Vaklinova, K. Kern, M. Burghard and A. Holleitner, *Nano Lett.*, 2017, **17**, 973–979.
81 S. M. Young, S. Zaheer, J. C. Y. Teo, C. L. Kane, E. J. Mele and A. M. Rappe, *Phys. Rev. Lett.*, 2012, 5.
82 T. Liang, Q. Gibson, M. N. Ali, M. Liu, R. J. Cava and N. P. Ong, *Nat. Mater.*, 2015, **14**, 5.
83 P. J. W. Moll, N. L. Nair, T. Helm, A. C. Potter, I. Kimchi, A. Vishwanath and J. G. Analytis, *Nature*, 2016, **535**, 266–270.
84 C. Zhang, A. Narayan, S. Lu, J. Zhang, H. Zhang, Z. Ni, X. Yuan, Y. Liu, J.-H. Park, E. Zhang, W. Wang, S. Liu, L. Cheng, L. Pi, Z. Sheng, S. Sanvito and F. Xiu, *Nat. Commun.*, 2017, **8**, 1272.
85 C. Zhang, Y. Zhang, X. Yuan, S. Lu, J. Zhang, A. Narayan, Y. Liu, H. Zhang, Z. Ni, R. Liu, E. S. Choi, A. Suslov,

© 2023 The Author(s). Published by the Royal Society of Chemistry

Open Access Article. Published on 04 2023. Downloaded on 20.10.24 7:31:28.
This article is licensed under a Creative Commons Attribution 3.0 Unported Licence.

S. Sanvito, L. Pi, H.-Z. Lu, A. C. Potter and F. Xiu, *Nature*, 2019, **565**, 331–336.
86 S. Chi, Z. Li, Y. Xie, Y. Zhao, Z. Wang, L. Li, H. Yu, G. Wang, H. Weng, H. Zhang and J. Wang, *Adv. Mater.*, 2018, 7.
87 Z. Wang, H. Weng, Q. Wu, X. Dai and Z. Fang, *Phys. Rev. B: Condens. Matter Mater. Phys.*, 2013, **88**, 125427.
88 A. D. Rice, C. H. Lee, B. Fluegel, A. G. Norman, J. N. Nelson, C. S. Jiang, M. Steger, D. L. McGott, P. Walker and K. Alberi, *Adv. Funct. Mater.*, 2022, **32**, 2111470.
89 M. N. Ali, Q. Gibson, S. Jeon, B. B. Zhou, A. Yazdani and R. J. Cava, *Inorg. Chem.*, 2014, **53**, 4062–4067.
90 Z. Wang, H. Weng, Q. Wu, X. Dai and Z. Fang, *Phys. Rev. B: Condens. Matter Mater. Phys.*, 2013, **88**, 125427.
91 Z. K. Liu, J. Jiang, B. Zhou, Z. J. Wang, Y. Zhang, H. M. Weng, D. Prabhakaran, S.-K. Mo, H. Peng, P. Dudin, T. Kim, M. Hoesch, Z. Fang, X. Dai, Z. X. Shen, D. L. Feng, Z. Hussain and Y. L. Chen, *Nat. Mater.*, 2014, **13**, 677–681.
92 A. Mosca Conte, O. Pulci and F. Bechstedt, *Sci. Rep.*, 2017, **7**, 45500.
93 Q. Wang, C.-Z. Li, S. Ge, J.-G. Li, W. Lu, J. Lai, X. Liu, J. Ma, D.-P. Yu, Z.-M. Liao and D. Sun, *Nano Lett.*, 2017, **17**, 834–841.
94 X. Yao, S. Zhang, Q. Sun, P. Chen, X. Zhang, L. Zhang, J. Zhang, Y. Wu, J. Zou, P. Chen and L. Wang, *ACS Photonics*, 2021, **8**, 1689–1697.
95 M. Yang, J. Wang, J. Han, J. Ling, C. Ji, X. Kong, X. Liu, Z. Huang, J. Gou, Z. Liu, F. Xiu and Y. Jiang, *ACS Photonics*, 2018, **5**, 3438–3445.
96 M. Yang, J. Wang, Y. Yang, Q. Zhang, C. Ji, G. Wu, Y. Su, J. Gou, Z. Wu, K. Yuan, F. Xiu and Y. Jiang, *J. Phys. Chem. Lett.*, 2019, **10**, 3914–3921.
97 Y. Yang, J. Zhou, X. Xie, X. Zhang, Z. Li, S. Liu, L. Ai, Q. Ma, P. Leng, M. Zhao, J. Wang, Y. Shi and F. Xiu, *ACS Nano*, 2022, 9.
98 M. Yan, H. Huang, K. Zhang, E. Wang, W. Yao, K. Deng, G. Wan, H. Zhang, M. Arita, H. Yang, Z. Sun, H. Yao, Y. Wu, S. Fan, W. Duan and S. Zhou, *Nat. Commun.*, 2017, **8**, 257.
99 M. S. Bahramy, O. J. Clark, B.-J. Yang, J. Feng, L. Bawden, J. M. Riley, I. Marković, F. Mazzola, V. Sunko, D. Biswas, S. P. Cooil, M. Jorge, J. W. Wells, M. Leandersson, T. Balasubramanian, J. Fujii, I. Vobornik, J. E. Rault, T. K. Kim, M. Hoesch, K. Okawa, M. Asakawa, T. Sasagawa, T. Eknapakul, W. Meevasana and P. D. C. King, *Nat. Mater.*, 2018, **17**, 21–28.
100 H. Xu, C. Guo, J. Zhang, W. Guo, C. Kuo, C. S. Lue, W. Hu, L. Wang, G. Chen, A. Politano, X. Chen and W. Lu, *Small*, 2019, **15**, 1903362.
101 X.-W. Tong, Y.-N. Lin, R. Huang, Z.-X. Zhang, C. Fu, D. Wu, L.-B. Luo, Z.-J. Li, F.-X. Liang and W. Zhang, *ACS Appl. Mater. Interfaces*, 2020, **12**, 53921–53931.
102 M. S. Shawkat, S. B. Hafiz, M. M. Islam, S. A. Mofid, M. M. Al Mahfuz, A. Biswas, H.-S. Chung, E. Okogbue, T.-J. Ko, D. Chanda, T. Roy, D.-K. Ko and Y. Jung, *ACS Appl. Mater. Interfaces*, 2021, **13**, 15542–15550.
103 W. Yu, Z. Dong, H. Mu, G. Ren, X. He, X. Li, S. Lin and K. Zhang, *ACS Nano*, 2022, 8.
104 J. Jiang, Y. Guo, X. Weng, F. Long, Y. Xin, Y. Lu, Z. Ye, S. Ruan and Y.-J. Zeng, *J. Mater. Chem. C*, 2021, **9**, 4978–4988.
105 K. Zhang, M. Yan, H. Zhang, H. Huang, M. Arita, Z. Sun, W. Duan, Y. Wu and S. Zhou, *Phys. Rev. B*, 2017, **96**, 125102.
106 X. Yu, P. Yu, D. Wu, B. Singh, Q. Zeng, H. Lin, W. Zhou, J. Lin, K. Suenaga, Z. Liu and Q. J. Wang, *Nat. Commun.*, 2018, **9**, 1545.
107 X. X. Feng, B. Liu, M. Long, M. Cai, Y. Peng and J. Yang, *J. Phys.: Condens. Matter*, 2020, **32**, 445004.
108 Y. Yang, J. Li, S. Choi, S. Jeon, J. H. Cho, B. H. Lee and S. Lee, *Appl. Phys. Lett.*, 2021, **118**, 013103.
109 L. Zeng, S. Lin, Z. Lou, H. Yuan, H. Long, Y. Li, W. Lu, S. P. Lau, D. Wu and Y. H. Tsang, *NPG Asia Mater.*, 2018, **10**, 352–362.
110 J. Lai, X. Liu, J. Ma, Q. Wang, K. Zhang, X. Ren, Y. Liu, Q. Gu, X. Zhuo, W. Lu, Y. Wu, Y. Li, J. Feng, S. Zhou, J.-H. Chen and D. Sun, *Adv. Mater.*, 2018, **30**, 1707152.
111 Y. Sun, S.-C. Wu, M. N. Ali, C. Felser and B. Yan, *Phys. Rev. B: Condens. Matter Mater. Phys.*, 2015, 7.
112 Z. Wang, D. Gresch, A. A. Soluyanov, W. Xie, S. Kushwaha, X. Dai, M. Troyer, R. J. Cava and B. A. Bernevig, *Phys. Rev. Lett.*, 2016, **117**, 056805.
113 Q. Yang, X. Wang, Z. He, Y. Chen, S. Li, H. Chen and S. Wu, *Adv. Sci.*, 2023, **10**, 2205609.
114 J. Lai, Y. Liu, J. Ma, X. Zhuo, Y. Peng, W. Lu, Z. Liu, J. Chen and D. Sun, *ACS Nano*, 2018, **12**, 4055–4061.
115 X. Han, P. Wen, L. Zhang, W. Gao, H. Chen, F. Gao, S. Zhang, N. Huo, B. Zou and J. Li, *ACS Appl. Mater. Interfaces*, 2021, **13**, 61544–61554.
116 J. Liu, F. Xia, D. Xiao, F. J. García De Abajo and D. Sun, *Nat. Mater.*, 2020, **19**, 830–837.
117 J. Liu and T. Hesjedal, *Adv. Mater.*, 2023, **35**, 2102427.
118 Y. Tokura, K. Yasuda and A. Tsukazaki, *Nat. Rev. Phys.*, 2019, **1**, 126–143.
119 H. Li, S. Ruan and Y. Zeng, *Adv. Mater.*, 2019, **31**, 1900065.
120 M. A. Iqbal, H. Xie, L. Qi, W. Jiang and Y. Zeng, *Small*, 2023, **19**, 2205347.
121 L. Qi, S. Ruan and Y. Zeng, *Adv. Mater.*, 2021, **33**, 2005098.


© 2023 The Author(s). Published by the Royal Society of Chemistry